



## Removal of tetracycline antibiotic from aqueous environments using core-shell silica magnetic nanoparticles

Nafiseh Farhadian\*, Mohammad Sadegh Rezaeian, Sona Aseyednezhad, Farideh Haffar, Saba Mehrad Fard

*Ferdowsi University of Mashhad, Faculty of Engineering, Chemical Engineering Department, Mashhad, Iran. P.O. Box: 9177948974, Tel.+985138805140, Fax +985138816840, email: n.farhadian@um.ac.ir (N. Farhadian), msrd1372@gmail.com (M.S. Rezaeian), sona.aseyednejad@gmail.com (S. Aseyednezhad), faridehhaffar@yahoo.com (F. Haffar), saba.mehrad69@yahoo.com (S.M. Fard)*

Received 5 January 2017; Accepted 10 May 2017

### ABSTRACT

The aim of this study is to investigate the removal of tetracycline (TC) antibiotics from aqueous solutions using core-shell magnetic nanoparticles. Fe<sub>3</sub>O<sub>4</sub> magnetic nanoparticles (NP) were synthesized using the solvothermal method. A silica core shell was coated on the NP surface by a modified stober sol-gel process. FTIR, TEM, VSM, and XRD analysis confirmed the formation of core shell magnetic NP with a size of 90 nm. In addition, tetracycline adsorption was applied to the synthesized NP under optimum adsorption conditions to enhance pollutant removal efficiency from water. Results showed that the maximum adsorption capacity ( $q_m$ ) of TC on the core-shell magnetic nanoparticles was enhanced by about 50% in comparison to uncoated magnetic nanoparticles. This adsorption capacity enhancement was due to the prevention of clustering and aggregation of adsorbents as well as stronger interactions between NP surfaces and TC molecules. Kinetic and isotherm studies showed that the adsorption behavior of TC on both adsorbents fitted well with the pseudo-second-order kinetics and Langmuir isotherm models, respectively. This confirmed the strong interaction between adsorbent and pollutant by forming a single layer of TC on the adsorbent surface. Finally, results suggested that coating the surface of iron oxide magnetic nanoparticles with silica improved the pollutant adsorption efficiency in aqueous media.

*Keywords:* Magnetic nanoparticles; Tetracycline removal; Adsorption; Non porous silica; Core-shell

### 1. Introduction

Nowadays, one of the most crucial environmental problems is water pollution caused by urbanization, industrialization, agriculture and pharmaceuticals [1]. Among pharmaceutical compounds, antibiotics represent a significant group of medical substances which are widely used in human therapy and veterinary medicine [2]. Since most of these antibiotics are defectively metabolized in the consumer's body, up to 90% of them are excreted virtually unchanged through urination and feces [3]. These residual antibiotics inflict critical adverse effects on human health and environment [4]. A major side effect of these bioactive compounds is the incidence of antibiotic

resistances among bacterial populations [5]. Also, these antibiotics are released from sewage treatment centers and agricultural runoff into the surface water and pollute the aquatic environment [4,6–8]. The tetracycline (TC) ranks second in terms of production and usage drugs among 25 commonly used antibiotics [9]. Disruption in respiration of soil microbes [10], reduction of Fe<sup>+3</sup> ion [11], nitrification of bacteria [12] and phosphatase enzyme activity [10] are some other serious consequences of TC accumulation in the environment. With respect to the cited negative effects of residual pharmaceuticals, the removal of tetracycline from the human food chain and water resources has grown into a vital concern since in the decades [13]. So far, several chemical and physical methodologies for the removal of antibiotics from aquatic environments have been investi-

\*Corresponding author.

gated which include conventional techniques (biological processes, filtration, coagulation, flocculation and sedimentation), advanced oxidation processes (AOPs), membrane processes, adsorption, etc. [14]. Low initial cost, convenient operation, ease of design, lack of sensitivity to poisonous compounds and application in a wide range of different solid sorbents such as nanoparticles, activated carbon, clays, carbon nanotubes and metal oxides make the adsorption process more efficient and attractive than other techniques [15,16]. Among various types of nanoparticles,  $\text{Fe}_3\text{O}_4$  magnetic nanoparticles (MNPs) are efficient adsorbents due to their high specific surface area, strong adsorption capability, adequate stability and facile preparation, operation and resumption [17]. However, the most important feature of these adsorbents is their superparamagnetic properties which distinguish them from other adsorbents. For example, despite high adsorption affinity of carbon nanotubes, a time-consuming separation step such as filtration or centrifugation is required after the adsorption process [18]. In the case of applying MNPs, this slow separation step can be substituted with a quick and straightforward stage using an external magnetic field similar to that of a magnet [19].

Recently, the role of magnetic materials in removing antibiotics has been investigated. Shi et al. synthesized a new magnetic mesoporous carbon composite ( $\text{Fe}_3\text{O}_4/\text{C}$ ) and studied its performance in removing Ciprofloxacin (CIP) antibiotics. They found that the maximum adsorption of CIP could be reached under neutral condition near to 98.28 mg/g [18]. Kakavandi et al. combined powder activated carbon (PAC) with  $\text{Fe}_3\text{O}_4$  MNPs to remove amoxicillin (AMX) from an aqueous solution, with their results showing a maximum adsorption capacity of 142.85 mg/g [20]. There are a number of studies on TCs removal from aqueous environment. In 2011, Zhang et al. employed  $\text{Fe}_3\text{O}_4$  MNPs for the removal of chlorotetracycline (CTC) from aqueous media [17].

However,  $\text{Fe}_3\text{O}_4$  magnetic nanoparticles suffer from disadvantages such as low binding capacity of target molecule, susceptibility to oxidation when exposed to air and tendency to aggregate into large clusters [21,22]. To overcome such limitations, the surface of these MNPs needs to be modified. Recent studies have shown that coating MNPs by silica materials offer an excellent alternative for adsorption and separation process [23–26]. In addition, the silica coating of iron oxide nanoparticles improve their chemical stability by preventing their aggregation in the liquid.

The primary goal of this study was the synthesis and characterization of  $\text{Fe}_3\text{O}_4$  magnetic nanoparticles along with core shell MNPs preparation. It was then followed by an analysis of the removal ability of each adsorbent ( $\text{Fe}_3\text{O}_4$  and  $\text{Fe}_3\text{O}_4@\text{SiO}_2$  MNPs) for TC separation from aqueous environment. A review of literature revealed the paucity of studies on TC removal from aqueous environment using silica coated MNPs ( $\text{Fe}_3\text{O}_4@\text{SiO}_2$  MNPs). This is the main contribution of this study. Also, the TC adsorption mechanism on both  $\text{Fe}_3\text{O}_4$  and  $\text{Fe}_3\text{O}_4@\text{SiO}_2$  MNPs was investigated in details by calculating adsorption isotherms and kinetics models. Furthermore, the optimum separation conditions to achieve highest removal efficiency for each adsorbent was examined.

## 2. Materials and methods

### 2.1. Materials

Iron (III) chloride hexahydrate ( $\text{FeCl}_3 \cdot 6\text{H}_2\text{O}$ ), sodium acetate anhydrous (NaAc), ethylene glycol (EG), 1,2-ethylenediamine (ETH), ethanol, ammonia (25–28%), tetraethoxysilane (TEOS), standard HCl and NaOH (0.1 N) were purchased from Merck Company. Tetracycline powder was obtained from Sigma–Aldrich Company.

### 2.2. Synthesis of magnetic $\text{Fe}_3\text{O}_4$ nanoparticles

Magnetic nanoparticles (MNPs) were prepared using the solvothermal method [27]. 1 g of  $\text{FeCl}_3 \cdot 6\text{H}_2\text{O}$  was dissolved in 30 mL of EG to make a clear solution. Then, 3g of NaAc and 10 mL of ETH were added to the solution. The mixture was vigorously stirred for 30 min and then transferred to a Teflon-lined stainless-steel autoclave and sealed to be heated at 200°C. After 8 h of reaction, the autoclave was cooled to the room temperature. The resultant black magnetite particles were washed with acetone and water several times before being dried at the room temperature.

### 2.3. Synthesis of $\text{Fe}_3\text{O}_4@\text{SiO}_2$ nanocomposite

The core-shell structured  $\text{Fe}_3\text{O}_4@\text{SiO}_2$  nanoparticles were synthesized by a modified Stober sol-gel process [28]. 0.1 g of synthesized  $\text{Fe}_3\text{O}_4$  nanoparticles were treated using 50 mL of HCl (0.1 M) solution under ultra-sonication for 20 min. Subsequently, the treated particles were collected by a magnet, washed with deionized water, and then dispersed in a mixture solution of ethanol (80 mL), deionized water (20 mL) and concentrated aqueous ammonia (1.0 mL) (28 wt.%). Then, 0.1 g of TEOS was added dropwise to the solution. After 6 h of stirring at the room temperature, the product was collected with a magnet and washed several times with ethanol and water before being dried at 60°C for 6 h.

### 2.4 Characterization

The transmission electron microscopy (TEM) images were taken by a CM 120 (Philips Holland) transmission electron microscope at a working temperature of 20°C and a voltage of 120 kV. The X-ray diffraction (XRD) patterns of the prepared magnetic silica nanocomposites were achieved at the room temperature by a X'Pert Pro MPD x-ray powder diffractometer (PANalytical Holland), operating with  $\text{Cu K}\alpha$  radiation ( $\lambda = 1.5406 \text{ \AA}$ ) of 40 kV and 40 mA. UV–visible absorption spectra were recorded using a CE 8000 double beam spectrophotometer (CECIL-CE9500). Fourier transform infrared (FT-IR) spectra ( $4000\text{--}400 \text{ cm}^{-1}$ ) were collected on a shimadzo co 370 FTIR spectrometer. The magnetic property of the magnetite nanoparticle was investigated by a vibrating sample magnetometer (VSM) using Lakeshore 7400 VSM. The zeta potentials were measured at the temperature (25°C) by dynamic light scattering (Nano-ZS, Malvern Instruments, England).

### 2.5. Determination of the point zero charge pH ( $\text{pH}_{\text{PZC}}$ )

To measure  $\text{pH}_{\text{PZC}}$  values, the pH drift method was applied [29]. Accordingly, samples were dispersed in low

ionic-strength aqueous media to reach equilibration and then any shift in pH values was measured to calculate  $\text{pH}_{\text{PZC}}$ . To this purpose, a solution containing 0.1 mol L<sup>-1</sup> NaCl and 10 ml test tubes was adjusted to pH values of 2–8 ( $\text{pH}_{\text{initial}}$ ) using NaOH and HCl. In the next step, 10 mg of each adsorbent was added to test tubes and shaken at 298 K. After 4 h, the final pH ( $\text{pH}_{\text{final}}$ ) of samples was measured by a microprocessor pH meter (pH 211, Hanna Instruments, Inc.) and plotted against initial pH. The intersection point of the resulting curve with the line passing origin ( $\text{pH}_{\text{final}} = \text{pH}_{\text{initial}}$ ) yields  $\text{pH}_{\text{PZC}}$ .

## 2.6. Batch experiments

One factorial experiments was performed to assess optimum adsorption parameters to achieve the maximum removal efficiency of TC. Also, pH, contact time and initial concentration of pollutant (TC) were reviewed in the batch mode of operation. In all experiments, the adsorbent mass and solution volume were assumed constant at 10 mg and 10 mL, respectively. To study the impact of initial pH of solution on adsorption, pH was modified from 3 to 8. Contact times varied from 30 min to 4 h. Experiments were performed at a constant temperature of 298 K and initial pollutant concentration of 100 ppm. To examine the effect of pollutant concentration on the removal efficiency, a standard stock solution of TC with 200 ppm concentration was produced. The initial concentration of TC varied from 20 ppm to 200 ppm depending on the dilution of the initial stock solution.

## 2.7. Batch adsorption

10 mg of adsorbent was added to 10 ml of the initial solution. The resultant solution was dispersed for 15 min by ultrasonic bath and mixed for a specific contact time on the magnetic stirrer. Finally, the solution was separated from NPs using an external magnetic field. The concentration of TC was determined by a calibration curve for UV-visible spectrophotometer at a wave-length of  $\lambda = 275$  nm [30] (see supporting file, S1 and S2). TC removal efficiency and adsorption capacity ( $q_e$  (mg·g<sup>-1</sup>)) can be calculated by the following equations, respectively [31]:

$$\text{TC removal efficiency \%} = \frac{C_0 - C_e}{C_0} \times 100 \quad (1)$$

$$q_e = \frac{C_0 - C_e}{M} \times v \quad (2)$$

where  $C_0$  represents the initial concentration of TC solution (mg·L<sup>-1</sup>),  $C_e$  is the concentration of solute in the bulk phase at the equilibrium (mg·L<sup>-1</sup>),  $v$  is the volume of aqueous phase (L) and  $M$  is the mass of nanoparticle (g).

## 2.8. Adsorption isotherms

In the present study, the Langmuir and the Freundlich isotherm models were used to depict the adsorption of TC onto both adsorbents.

In the Langmuir isotherm, a monolayer adsorption on a surface consisting of identical binding sites with compara-

ble adsorption energies and non-interaction between adsorbate was assumed.

The linear form of Langmuir equation can be expressed as follows [32]:

$$\frac{C_e}{q_e} + \frac{C_e}{q_{\text{max}}} + \frac{1}{q_{\text{max}}k_L} \quad (3)$$

where  $C_e$  is the equilibrium concentration of the solution (mg/L),  $q_{\text{max}}$  is the maximum adsorption capacity (mg/g), and  $k_L$  is the Langmuir constant for the affinity of binding sites and adsorption energy (L/g). The Langmuir constants can be obtained from  $C_e/q_e$  vs.  $C_e$  plot.

The Freundlich isotherm is an empirical equation based upon the assumption of heterogeneous surface energies. The linear form of the equation is expressed as follows [32]:

$$\ln q_e = \ln k_f + \frac{1}{n} \ln C_e \quad (4)$$

where  $k_f$  is the Freundlich constant of the adsorption capacity (L/g) and  $1/n$  is an empirical parameter related to adsorption intensity. The Freundlich constant can be calculated from the plots of  $\ln q_e$  vs.  $\ln C_e$ .

## 2.9. Adsorption kinetics

In this study, pseudo-first-order and pseudo-second-order kinetics were used for the modelling of the experimental adsorption kinetic data, the linear forms of which are represented below:

Pseudo-first-order model,

$$\ln \left( \frac{q_e - q_t}{q_e} \right) = -k_1 t \quad (5)$$

Pseudo-second-order model,

$$\frac{t}{q_t} = \frac{1}{k_2 q_e^2} + \frac{1}{q_e} t \quad (6)$$

where  $q_e$  is the amount of adsorbate at equilibrium (mg/g),  $q_t$  is the amount of adsorbate at each time (mg/g),  $k_1$  and  $k_2$  are the first and second order equilibrium rate constants, respectively. The former constant was determined based on the slope of linear plot of  $\ln(q_e - q_t)$  vs. time and the latter was calculated by plotting the kinetic data of  $t/q_t$  vs.  $t$ .

## 3. Results and discussion

### 3.1. Synthesis and characterization of Fe<sub>3</sub>O<sub>4</sub>@nSiO<sub>2</sub>

Initially, it is necessary to confirm the formation of magnetic nanoparticle and silica coated on particles. To do so, XRD patterns of both Fe<sub>3</sub>O<sub>4</sub> and Fe<sub>3</sub>O<sub>4</sub>@nSiO<sub>2</sub> MNPs are presented in Fig. 1. As shown in Fig. 1a, the diffraction peaks at 2 $\theta$  values of 18.30°, 30.20°, 35.55°, 43.26°, 57.21° and 62.87° represent the amorphous structure of iron oxide MNPs [33]. In addition, the broad peak at 20°–30° angles confirm the existence of amorphous SiO<sub>2</sub> coating (Fig. 1b) [34]. Also, Fig. 1b suggests that silica coating does not considerably change the structure of MNPs.

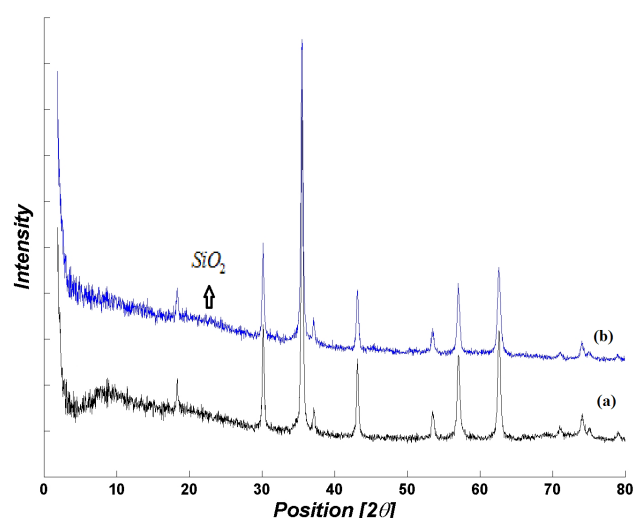


Fig. 1. XRD patterns of (a)  $\text{Fe}_3\text{O}_4$  and (b)  $\text{Fe}_3\text{O}_4@n\text{SiO}_2$  MNPs.

The FTIR spectra of  $\text{Fe}_3\text{O}_4$  and  $\text{Fe}_3\text{O}_4@n\text{SiO}_2$  are shown in Fig. 2. The absorption peaks around 565–570  $\text{cm}^{-1}$  in both figures, which correspond to Fe–O vibration bond, are related to the magnetite phase [31]. In Fig. 2b, the broad high-intensity band at 1097  $\text{cm}^{-1}$  could be associated with the oxygen motion in Si–O–Si anti-symmetric stretch, which is due to asymmetric stretching bonds of Si–O–Si in  $\text{SiO}_2$  [35]. The peak around 793  $\text{cm}^{-1}$  is related to Si–O–Si symmetric stretching bond [30], whereas the peak around 466  $\text{cm}^{-1}$  corresponds to Si–O–Si or O–Si–O bending modes [35]. The peaks at 947  $\text{cm}^{-1}$  is due to the Si–O symmetric stretching [35].

The structure and morphology of the magnetic silica nanocomposites were investigated using TEM analysis. Fig. 3 shows the typical TEM images of  $\text{Fe}_3\text{O}_4@n\text{SiO}_2$ . Clearly, the nanocomposites have a core-shell structure with a dark contrast core of  $\text{Fe}_3\text{O}_4$  and a light contrast of silica shell which indicate the successful coating of  $\text{Fe}_3\text{O}_4$  nanoparticles by a nonporous silica shell. The initial  $\text{Fe}_3\text{O}_4$  particles are uniform with a mean diameter of 70 nm. The estimated thickness of the nonporous silica shell was around 10 nm, based on contrast between the core and shell regimes.

Magnetization curves, as shown in Fig. 4, were measured in powder samples of  $\text{Fe}_3\text{O}_4$  and  $\text{Fe}_3\text{O}_4@n\text{SiO}_2$  nanoparticles at room temperature relative to the change of applied magnetic field (Oe) from –10000 Oe to 10000 Oe. Both  $\text{Fe}_3\text{O}_4$  nanoparticles and  $\text{Fe}_3\text{O}_4@n\text{SiO}_2$  nanocomposites exhibited negligible coercivity and remanence in the absence of the magnetic field. The super paramagnetic behavior of samples can lead to the dispersion of particles in the solution without any magnetic interactions between particles and magnetic clustering. The saturation magnetizations of  $\text{Fe}_3\text{O}_4$  nanoparticles and  $\text{Fe}_3\text{O}_4@n\text{SiO}_2$  nanocomposites were 69.5  $\text{emu/g}$  and 52.3  $\text{emu/g}$ , respectively. The reduced saturation magnetization was due to the relatively lower density of magnetic components in nanocomposites as silica coated on the  $\text{Fe}_3\text{O}_4$  nanoparticles. Additionally, no hysteresis was observed on the magnetization curves of all samples, indicating the superparamagnetic character of

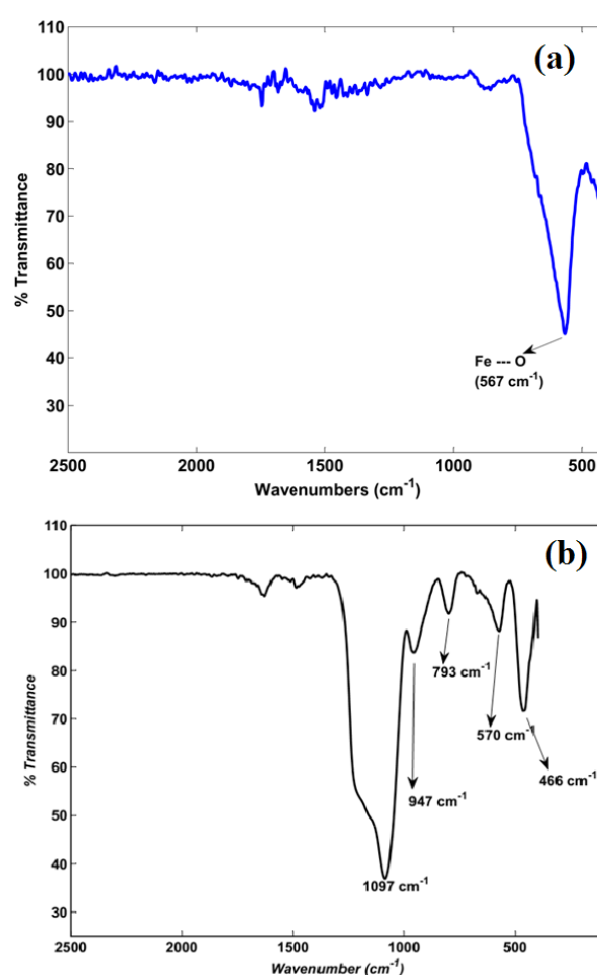


Fig. 2. FT-IR spectrums of (a)  $\text{Fe}_3\text{O}_4$  and (b)  $\text{Fe}_3\text{O}_4@n\text{SiO}_2$  MNPs.

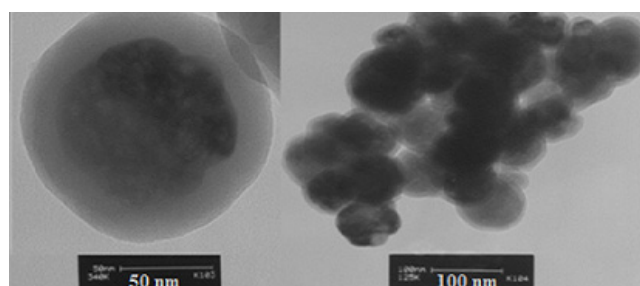


Fig. 3. TEM images of  $\text{Fe}_3\text{O}_4@n\text{SiO}_2$ .

these materials. The characterization results are consistent with the literature [36].

### 3.2. Adsorption parameter effect

#### 3.2.1. Analysis of pH<sub>PZC</sub>

Fig. 5 illustrates curves of  $\text{pH}_{\text{final}}$  vs.  $\text{pH}_{\text{initial}}$  for  $\text{Fe}_3\text{O}_4$  and  $\text{Fe}_3\text{O}_4@n\text{SiO}_2$  MNPs with corresponding  $\text{pH}_{\text{PZC}}$  values of 7

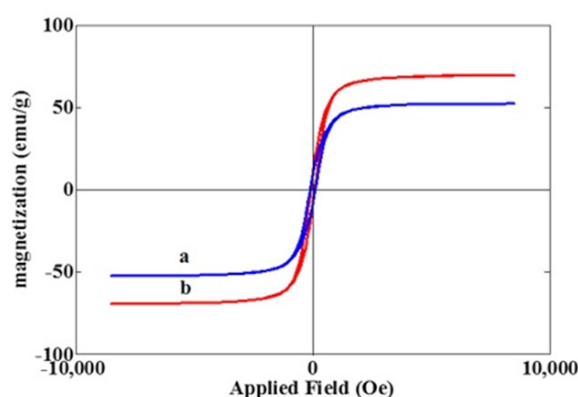


Fig. 4. Magnetization curves of (a)  $\text{Fe}_3\text{O}_4$  and (b)  $\text{Fe}_3\text{O}_4@\text{nSiO}_2$ .

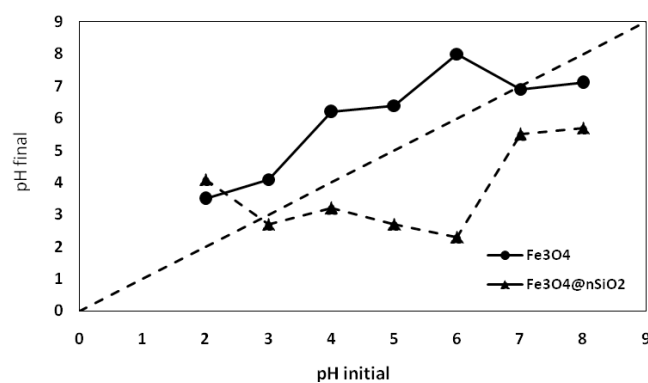


Fig. 5. pHpzc of  $\text{Fe}_3\text{O}_4$  and  $\text{Fe}_3\text{O}_4@\text{nSiO}_2$  MNPs.

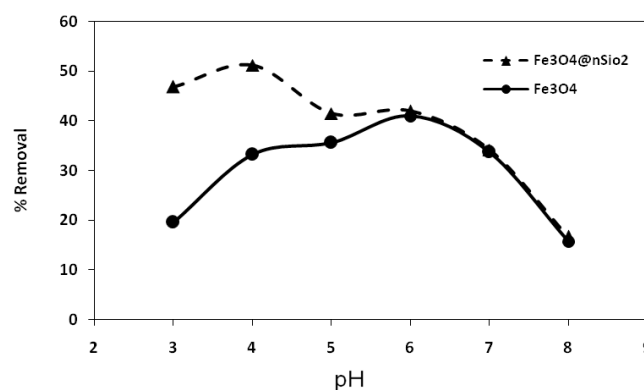


Fig. 6. Effect of pH on the adsorption rate of TC on both  $\text{Fe}_3\text{O}_4$  and  $\text{Fe}_3\text{O}_4@\text{nSiO}_2$  NP at initial concentration of 100 ppm.

and 2.8, respectively. The  $\text{pH}_{\text{PZC}}$  values calculated for adsorbents are in agreement with previous studies [17,37].

### 3.2.2. Effect of solution pH

The effect of pH on the adsorption rate of TC on both adsorbents ( $\text{Fe}_3\text{O}_4$  and  $\text{Fe}_3\text{O}_4@\text{nSiO}_2$ ) are shown in Fig. 6. As can be seen, the adsorption ability of NPs is a variable of pH. The maximum adsorption of TC by  $\text{Fe}_3\text{O}_4$  MNPs and  $\text{Fe}_3\text{O}_4@\text{nSiO}_2$  is achieved at pH 6 and 4, respectively. The observed pH dependence could be rationalized by evaluating the charges of TC and adsorbents surfaces. TC is an amphoteric molecule with multiple ionisable functional groups. The pKa of TC molecule is 3.3, 7.68 and 9.69, respectively [38]. These pKa values suggest the existence of TC as a cationic ion in strong acid solution, zwitter anions at  $3.3 < \text{pH} < 7.7$ , and negative ions at  $\text{pH} > 7.7$ . The estimated zero point of charge ( $\text{pH}_{\text{pzc}}$ ) for  $\text{Fe}_3\text{O}_4$  MNPs and  $\text{Fe}_3\text{O}_4@\text{nSiO}_2$  was 7 and 2.8, respectively. This indicates that  $\text{Fe}_3\text{O}_4$  MNP is positively charged at  $\text{pH} < 7$  and negatively charged at  $\text{pH} > 7$ . Therefore, the electrostatic repulsion between TC and  $\text{Fe}_3\text{O}_4$  surface was the lowest at pH near  $\text{pKa}_2$  ( $\text{pH} \approx 6$ ). However,  $\text{Fe}_3\text{O}_4@\text{nSiO}_2$  surface was positively charged at  $\text{pH} < 2.8$  and negatively charged at  $\text{pH} > 2.8$ . Therefore, electrostatic repulsion between TC and  $\text{Fe}_3\text{O}_4@\text{nSiO}_2$  surface was lowest at pH near  $\text{pKa}_1$  ( $\text{pH} \approx 4$ ). The results concerning

the relation between charges of TC and  $\text{Fe}_3\text{O}_4$  MNP surface are in agreement with previous studies [17,39].

### 3.2.3. Effect of contact time

The results of contact time at optimal pH value of each adsorbent are shown in Fig. 7. It should be noted that the main purpose of this study was to obtain the maximum removal efficiency of TC from aqueous media. Given that the electrostatic repulsion between TC and adsorbents ( $\text{Fe}_3\text{O}_4$  and  $\text{Fe}_3\text{O}_4@\text{nSiO}_2$ ) was different, the best pH values for maximum removal efficiency was selected for each adsorbents at different values based on the results of previous section. As shown in the figure, at initial contact time, the adsorption rate increased proportional to the rise of contact time, which persisted up to 2 h. However, after 2 h, an increase in contact time reduced TC adsorption rate. It is probably because at the initial contact time (up to 2 h), the surface active site was saturated with TC, but as the time lapsed, TC was desorbed from the surface of nanocomposites. This is due to weak interaction between drug molecules and nanocomposite surface. This observation was more significant for  $\text{Fe}_3\text{O}_4@\text{nSiO}_2$  adsorbent. It seems that the nature of interaction between silica surface

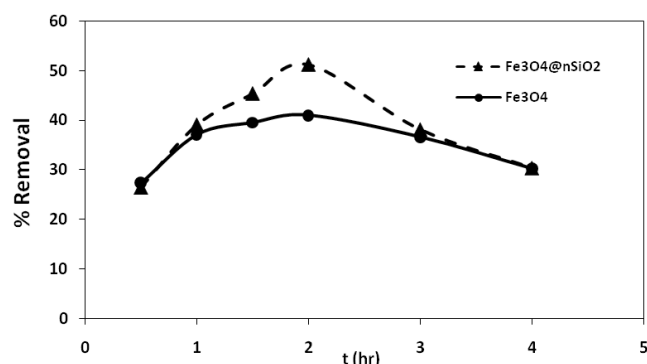


Fig. 7. Effect of contact time on the adsorption rate of TC on both Fe<sub>3</sub>O<sub>4</sub> and Fe<sub>3</sub>O<sub>4</sub>@nSiO<sub>2</sub> at the initial concentration of 100 ppm.

of Fe<sub>3</sub>O<sub>4</sub> and TC is distinct from that of Fe<sub>3</sub>O<sub>4</sub> surface and TC. As Fig. 7 shows, the difference between adsorption and desorption of TC over 1–4 h is only 5% for Fe<sub>3</sub>O<sub>4</sub>, but this value rises to about 15% for Fe<sub>3</sub>O<sub>4</sub>@nSiO<sub>2</sub>. This confirms the weak interaction between TC molecules, which were adsorbed later and adsorbent surface of Fe<sub>3</sub>O<sub>4</sub>@nSiO<sub>2</sub>. This feeble interaction between drug and adsorbent surface could be due to various adsorption sites on the adsorbent surface. However, further analyses using adsorption isotherm modeling are required to confirm the results. Therefore, 2 h was determined as the optimal exposure time to achieve maximum adsorption, which is in agreement with previous studies [40].

#### 3.2.4. Effect of pollutant initial concentration

To evaluate the effect of initial concentration of pollutant, the adsorption process for both adsorbents was investigated at the initial pollutant concentration of 20–200 ppm at optimal pH and contact time. The results are depicted in Figs. 8 and 9.

As shown in Fig. 8, with an increase in the initial concentration of TC, the driving force for mass transfer rises, and the saturation state of adsorbents is more promptly achieved. In other words, all adsorbents have a limited number of active sites, which are saturated at a certain concentration of pollutants [29]. This decreased the removal efficiency of TC at higher initial concentration of TC.

On the other hand, as illustrated in Fig. 9, higher initial concentration of TC resulted in greater adsorption capacity ( $q_e$ ). This was due to the fact that the greater concentration gradient accelerated mass transfer. Moreover, applying core-shell MNPs enhanced the adsorption capacity of TC by 1.5 times in comparison to Fe<sub>3</sub>O<sub>4</sub>, which due to enhanced dispersion of particles in the solution with stronger bonding capacity of TC and silica shell. This was also observed for adsorption of other drugs on Fe<sub>3</sub>O<sub>4</sub>@nSiO<sub>2</sub> core-shell nanoparticle [41].

### 3.3. Adsorption modelling

#### 3.3.1. Adsorption isotherms

Isotherm curves of Langmuir and Freundlich models and their estimated parameters are shown in Fig. 10 and

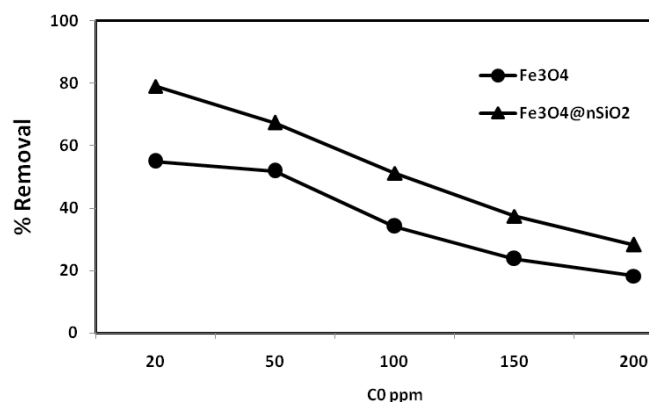


Fig. 8. Effect of initial concentration of TC on the removal efficiency.

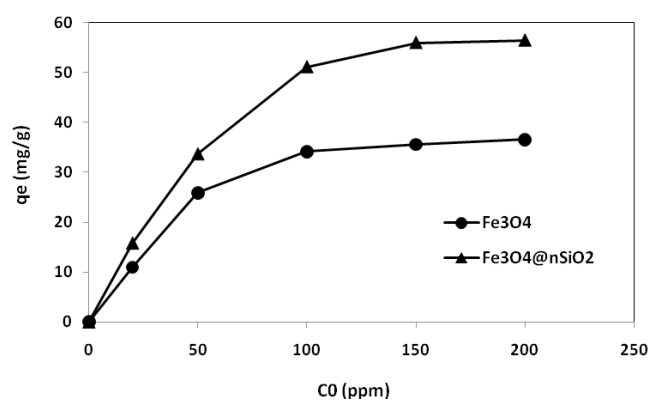


Fig. 9. Effect of initial concentration of TC on the adsorption capacity of both Fe<sub>3</sub>O<sub>4</sub> and Fe<sub>3</sub>O<sub>4</sub>@nSiO<sub>2</sub> adsorbents.

Table 1, respectively. According to results, Langmuir isotherm ( $R^2 > 0.996$ ) offers more efficient representation of data than does the Freundlich isotherm ( $R^2 > 0.776$ ) for Fe<sub>3</sub>O<sub>4</sub> MNP. This confirms a monolayer formation of TC on both MNPs, which is in agreement with the literature [17]. However, for Fe<sub>3</sub>O<sub>4</sub>@nSiO<sub>2</sub> MNPs, both Langmuir and Freundlich models could sufficiently predict the adsorption phenomena, which is consistent with previous studies [41]. The results display multilayer adsorptions on this adsorbent. This can affect the adsorption and desorption nature of TC, as shown in Fig. 7. In other words, TC molecules adsorbed on the second layer of the adsorbent could be removed from the surface conveniently. This makes a significant distinction between adsorption and desorption values of TC vs. time. Moreover, based on estimated parameters listed in Table 1, Fe<sub>3</sub>O<sub>4</sub>@nSiO<sub>2</sub> MNPs have higher adsorption capacity in comparison to Fe<sub>3</sub>O<sub>4</sub> MNPs.

By comparing the adsorption capacity of Fe<sub>3</sub>O<sub>4</sub>@nSiO<sub>2</sub> MNPs ( $q_{max} = 61.73$  mg/g) with other adsorbents such as Pumice stone ( $q_{max} = 20.02$  mg/g) [39], magnetic molecularly imprinted nanoparticles (MMINs) ( $q_{max} = 14.31$  mg/g) [40], Montmorillonite ( $q_{max} = 54$  mg/g) [42], Graphite ( $q_{max} = 4.5$  mg/g) [43], graphene oxide functionalized magnetic particles (GO-MPs) ( $q_{max} = 39.1$  mg/g) [44] and Kaolinite ( $q_{max}$

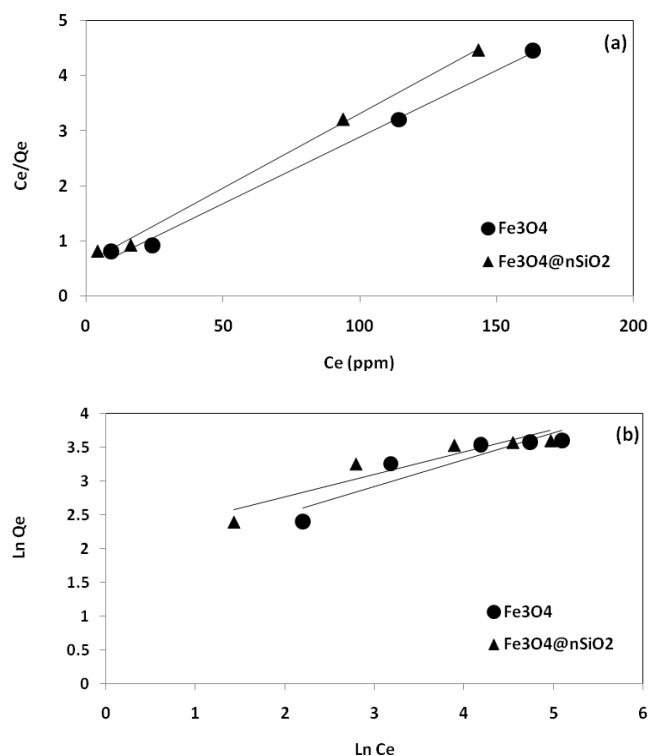


Fig. 10. (a) Langmuir and (b) Freundlich isotherm models for TC adsorption on both  $\text{Fe}_3\text{O}_4$  and  $\text{Fe}_3\text{O}_4@\text{nSiO}_2$  adsorbents.

Table 1

Langmuir and Freundlich isotherm parameters for TC adsorption on  $\text{Fe}_3\text{O}_4$  and  $\text{Fe}_3\text{O}_4@\text{SiO}_2$

|                                      | Langmuir             |                |       | Freundlich |                |       |
|--------------------------------------|----------------------|----------------|-------|------------|----------------|-------|
|                                      | $q_{\max}$<br>(mg/g) | $k_L$<br>(L/g) | $R^2$ | n          | $k_f$<br>(L/g) | $R^2$ |
| $\text{Fe}_3\text{O}_4$              | 41.67                | 0.05           | 0.996 | 2.49       | 5.82           | 0.776 |
| $\text{Fe}_3\text{O}_4@\text{SiO}_2$ | 61.73                | 0.08           | 0.999 | 2.73       | 10.61          | 0.935 |

= 4.32 mg/g) [45], it can be concluded that the proposed nanostructure has higher TC removal ability.

### 3.3.2. Adsorption kinetic

Fig. 11 represents the pseudo-first and pseudo-second-order kinetic curves for TC adsorption on both iron oxide MNPs. A summary of adsorption data by different kinetic models for two types of adsorbents are shown in Table 2. As shown in Fig. 11 and Table 2, the second-order kinetic model displays higher compliance with adsorption kinetic data than does the pseudo-first-order kinetic model, which is consistent with previous studies. [17].

## 4. Conclusions

This paper studied the separation of Tetracycline antibiotic from aqueous environment by applying the

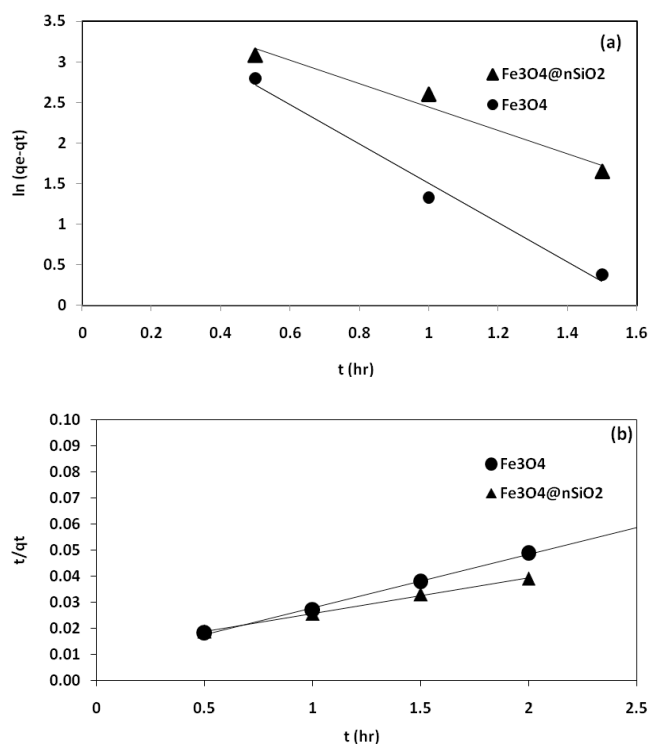


Fig. 11. TC adsorption kinetic models as (a) pseudo-first-order and (b) pseudo-second-order on both  $\text{Fe}_3\text{O}_4$  and  $\text{Fe}_3\text{O}_4@\text{nSiO}_2$  adsorbents.

Table 2

Pseudo-first and pseudo-second-order kinetic constants for TC adsorption on  $\text{Fe}_3\text{O}_4$  and  $\text{Fe}_3\text{O}_4@\text{SiO}_2$

|                                      | Pseudo-first-order |                   |       | Pseudo-second-order |                             |       |
|--------------------------------------|--------------------|-------------------|-------|---------------------|-----------------------------|-------|
|                                      | $q_e$<br>(g/mg)    | $k_1$<br>(g/mg h) | $R^2$ | $q_e$<br>(g/mg)     | $k_2$<br>(h <sup>-1</sup> ) | $R^2$ |
| $\text{Fe}_3\text{O}_4$              | 48.09              | 2.434             | 0.985 | 50                  | 0.057                       | 0.997 |
| $\text{Fe}_3\text{O}_4@\text{SiO}_2$ | 50.71              | 1.43              | 0.965 | 76.92               | 0.014                       | 0.998 |

adsorption process.  $\text{Fe}_3\text{O}_4$  magnetic nanoparticles and core shell MNP with silica ( $\text{Fe}_3\text{O}_4@\text{nSiO}_2$ ) were used for this purpose. This is the first adsorption study to apply core shell magnetic nanoparticles for pollutant removal. Results showed that core-shell magnetic nanoparticle could dramatically increase the adsorption capacity of adsorbents in comparison to unmodified  $\text{Fe}_3\text{O}_4$  MNP. This is due to stronger interactions between antibiotic and shell surface of nanoparticles. Moreover, nanoparticle coating with silica shell prevents clustering and aggregation of iron oxide MNPs, which increases the adsorption capacity of adsorbent. Adsorption modeling confirmed that the adsorption of TC on both types of adsorbents was monolayer. Furthermore, pseudo-second-order model revealed the chemical adsorption of TC onto both adsorbents. Finally, it could be concluded that coating the surface of MNPs significantly modify the adsorption properties of NPs.

## References

- [1] P.K. Geol, *Water Pollution: Causes, Effects and Control*, 2<sup>nd</sup>ed., New Delhi : New Age International, 2006.
- [2] M. Brigante, P.C. Schulz, Removal of the antibiotic TC by titania and titania-silica composed materials, *J. Hazard. Mater.*, 192 (2011) 1597–1608.
- [3] K.J. Choi, S.G. Kim, S.H. Kim, Removal of tetracycline and sulfonamide classes of antibiotic compound by powdered activated carbon, *Environ. Technol.*, 29(3) (2008) 333–342.
- [4] L. Zhang, X. Song, X. Liu, L. Yang, F. Pan, J. Lv, Studies on the removal of TC by multi-walled carbon nanotubes, *Chem. Eng. J.*, 178 (2011) 26–33.
- [5] J.C. Chee-Sanford, R.I. Aminov, I.J. Krapac, N. Garrigues-Jeanjean, R.I. Mackie, Occurrence and diversity of tetracycline resistance genes in lagoons and groundwater underlying two swine production facilities, *Appl. Environ. Microbiol.*, 67 (2001) 1494–1502.
- [6] E. Zuccato, R. Bagnati, F. Fioretti, M. Natangelo, D. Calamari, R. Fanelli, Environmental loads and detection of pharmaceuticals in Italy, in: K. Kummerer (Ed.), *Pharmaceuticals in the Environment. Sources, Fate, Effects and Risks*, Springer-Verlag, Berlin, Heidelberg, 2001.
- [7] A. Bruchet, C. Prompsy, G. Fillppi, A. Soual, A broad spectrum analytical scheme for the screening of endocrine disruptors (EDs), pharmaceuticals and personal care products in wastewaters and natural waters, *Water Sci. Technol.*, 46 (2002) 97–104.
- [8] D.W. Kolpin, E.T. Furlong, M.T. Meyer, E.M. Thurman, S.S.D. Zaugg, L.B. Barber, H.T. Buxton, Pharmaceuticals, hormones and other organic wastewater contaminants in US streams, 1999–2000: a national reconnaissance, *Environ. Sci. Technol.*, 36 (2002) 1202–1211.
- [9] M. Ghaemi, G. Absalan, Fast removal and determination of doxycycline in water samples and honey by Fe<sub>3</sub>O<sub>4</sub> magnetic nanoparticles, *J. Iranian Chem. Soc.*, 12(1) (2015) 1–7.
- [10] S. Boleas, C. Alonso, J. Pro, C. Fernández, G. Carbonell, J.V. Tarazona, Toxicity of the antimicrobial oxytetracycline to soil organisms in a multi-species-soil system (MS-3) and influence of manure co-addition, *J. Hazard. Mater.*, 122 (2005) 233–241.
- [11] S. Thiele-Bruhn, I.-C. Beck, Effects of sulfonamide and tetracycline antibiotics on soil microbial activity and microbial biomass, *Chemosphere*, 59 (2005) 457–465.
- [12] B. Halling-Sørensen, Inhibition of aerobic growth and nitrification of bacteria in sewage sludge by antibacterial agents, *Arch. Environ. Contam. Toxicol.*, 40 (2001) 451–460.
- [13] K. Kümmerer, Significance of antibiotics in the environment, *J. Antimicrob. Chemother.*, 52 (2003) 5–7.
- [14] V. Homem, L. Santos, Degradation and removal methods of antibiotics from aqueous matrices—a review, *J. Environ. Manage.*, 92 (2011) 2304–2347.
- [15] T. Sismanoglu, Y. Kismir, S. Karakus, Single and binary adsorption of reactive dyes from aqueous solutions onto clinoptilolite, *J. Hazard. Mater.*, 184 (2010) 164–169.
- [16] M. Bazregari, N. Farhadian, Modification the surface of MWCNT for improvement the amoxicilline removal from aqueous environment, MSc. Thesis, Ferdowsi University of Mashhad, Iran, 2015.
- [17] D. Zhang, N. Hongyun, X. Zhang, Z. Meng, Y. Cai, Strong adsorption of chlorotetracycline on magnetite nanoparticles, *J. Hazard. Mater.*, 192 (2011) 1088–1093.
- [18] S. Shi, Y. Fan, Y. Huang, Facile low temperature hydrothermal synthesis of magnetic mesoporous carbon nanocomposite for adsorption removal of ciprofloxacin antibiotics, *Ind. Eng. Chem. Res.*, 52 (2013) 2604–2612.
- [19] Q. Jiuhui, Research progress of novel adsorption processes in water purification: A review, *J. Environ. Sci.*, 20 (2008) 1–13.
- [20] B. Kakavandi, A. Esrafil, A. Mohseni-Bandpi, A. Jonidi Jafari R. Rezaei Kalantary, Magnetic Fe<sub>3</sub>O<sub>4</sub>@C nanoparticles as adsorbents for removal of amoxicillin from aqueous solution, *Water Sci. Technol.*, 69 (2014) 147–155.
- [21] J. Shi, L. Tong, D. Liu, H. Yang, Fabrication, structure, and properties of Fe<sub>3</sub>O<sub>4</sub>@C encapsulated with YVO<sub>4</sub>: Eu<sup>3+</sup> composites, *Nanoparticle Res.*, 14 (2012) 1–9.
- [22] A.L. Andrade, D.M. Souza, M.C. Pereira, J.D. Fabris, R.Z. Domingues, Synthesis and characterization of magnetic nanoparticles coated with silica through a sol-gel approach, *Cerâmica*, 55 (2009) 420–424.
- [23] L. Xu, J. Dai, J. Pan, X. Li, P. Huo, Y. Yan, X. Zou, R. Zhang, Performance of rattle-type magnetic mesoporous silica spheres in the adsorption of single and binary antibiotics, *Chem. Eng. J.*, 174 (2011) 221–230.
- [24] S.L.C. Pinho, G.A. Pereira, P. Voisin, J. Kassem, V. Bouchaud, L. Etienne, J.A. Peters, L. Carlos, S. Mornet, G.F.G.C. Geraldes, J. Rocha, M.H. Delville, Fine tuning of the relaxometry of  $\gamma$ -Fe<sub>2</sub>O<sub>3</sub>@SiO<sub>2</sub> nanoparticles by tweaking the silica coating thickness, *ACS Nano*, 4 (2010) 5339–5349.
- [25] M.J. Ding, X.L. Wu, L.H. Yuan, S. Wang, Y. Li, R.Y. Wang, T.T. Wen, S.H. Du, X.M. Zhou, Synthesis of core-shell magnetic molecularly imprinted polymers and detection of sildenafil and vardenafil in herbal dietary supplements, *J. Hazard. Mater.*, 191 (2011) 177–183.
- [26] H.M. Joshi, M. De, F. Richter, J. He, P.V. Prasad, V.P. Dravid, Effect of silica shell thickness of Fe<sub>3</sub>O<sub>4</sub>-SiO<sub>2</sub> core-shell nanostructures on MRI contrast, *Contrast Media Mol. Imaging*, 7 (2012) 460–468.
- [27] Sh. Guo, D. Li, L. Zhang, J. Li, E. Wang, Monodisperse mesoporous superparamagnetic single-crystal magnetite nanoparticles for drug delivery, *Biomater.*, 30 (2009) 1881–1889.
- [28] F. Liu, H. Tian, J. He, H. Liu, Efficient control over the pore structure of Fe<sub>3</sub>O<sub>4</sub>-nSiO<sub>2</sub>-mSiO<sub>2</sub> core-shell nanoparticles, *Int. J. Nanosci.*, 11 (2012) 1240031.
- [29] H. Pouretedal, N. Sadegh, Effective removal of Amoxicillin, Cephalixin, Tetracycline and Penicillin G from aqueous solutions using activated carbon nanoparticles prepared from vine wood, *J. Water Process Eng.*, 1 (2014) 64–73.
- [30] M.E. Parolo, M.C. Savini, J.M. Vales, M.T. Baschini, M.J. Avena, Tetracycline adsorption on montmorillonite: pH and ionic strength effects, *Appl. Clay Sci.*, 40 (2008) 179–186.
- [31] L.X. Zhou, S.D. Pan, X.H. Chen, Y.G. Zhao, B.B. Zou, M.C. Jin., Kinetics and thermodynamics studies of pentachlorophenol adsorption on covalently functionalized Fe<sub>3</sub>O<sub>4</sub>@SiO<sub>2</sub>-MWCNTs core-shell magnetic microspheres, *Chem. Eng. J.*, 257 (2014) 10–19.
- [32] S. Wu, X. Zhao, Y. Li, Q. Du, J. Sun, Y. Wang, X. Wang, Y. Xia, Z. Wang, L. Xia, Adsorption properties of doxorubicin hydrochloride onto graphene oxide: equilibrium, kinetic and thermodynamic studies, *Materials*, 6 (2013) 2026–2042.
- [33] F. Ahangaran, A. Hassanzadeh, S. Nouri, Surface modification of Fe<sub>3</sub>O<sub>4</sub>@SiO<sub>2</sub> microsphere by silane coupling agent, *Int. Nano Lett.*, 3(1) (2013) 23.
- [34] B. Sahoo, K. Sanjana, P. Devi, S. Kumar Sahu, Facile preparation of multifunctional hollow silica nanoparticles and their cancer specific targeting effect, *Biomater. Sci.*, 1(6) (2013) 647–657.
- [35] M. Zhang, A. Li, Q. Zhou, C. Shuang, W. Zhou, M. Wang, Effect of pore size distribution on tetracycline adsorption using magnetic hypercrosslinked resins, *Micropor. Mesopor. Mater.*, 184 (2014) 105–111.
- [36] J. Wang, S. Zheng, Y. Shao, J. Liu, Z. Xu, D. Zhu, Amino-functionalized Fe<sub>3</sub>O<sub>4</sub>@SiO<sub>2</sub> core-shell magnetic nanomaterial as a novel adsorbent for aqueous heavy metals removal, *J. Colloid Interface Sci.*, 349(1) (2010) 293–299.
- [37] S. Wang, J. Tang, H. Zhao, J. Wan, K. Chen, Synthesis of magnetite-silica core-shell nanoparticles via direct silicon oxidation, *J. Colloid Interface Sci.*, 432 (2014) 43–46.
- [38] X.-R. Xu, X.-Y. Li, Sorption and desorption of antibiotic tetracycline on marine sediments, *Chemosphere*, 78(4) (2010) 430–436.
- [39] U.A. Guler, M. Sarioglu, Removal of tetracycline from wastewater using pumice stone: equilibrium, kinetic and thermodynamic studies, *J. Environ. Health Sci. Eng.*, 12(1) (2014) 79.
- [40] J. Dai, J. Pan, L. Xu, X. Li, Z. Zhoe, R. Zhang, Y. Yan, Preparation of molecularly imprinted nanoparticles with superparamagnetic susceptibility through atom transfer radical emulsion polymerization for the selective recognition of tetracycline from aqueous medium, *J. Hazard. Mater.*, 205 (2012) 179–188.

- [41] S. MehradFard, N. Farhadian, T. Rohani-Bastami, M. Ebrahimi, M. Karimi, A. Allahyari, Synthesis, characterization and cellular cytotoxicity evaluation of a new magnetic nanoparticle carrier co-functionalized with amine and folic acid, *J. Drug Deliv. Sci. Technol.*, 38 (2017) 116–124.
- [42] R.A. Figueroa, A. Leonard, A.A. MacKay, Modeling tetracycline antibiotic sorption to clays, *Environ. Sci. Technol.*, 38(2) (2004) 476–483.
- [43] L. Ji, W. Chen, S. Zheng, Z. Xu, D. Zhu, Adsorption of sulfonamide antibiotics to multiwalled carbon nanotubes, *Langmuir*, 25(19) (2009) 11608–11613.
- [44] Y. Lin, S. Xu, J. Li, Fast and highly efficient tetracyclines removal from environmental waters by graphene oxide functionalized magnetic particles, *Chem. Eng. J.*, 225 (2013) 679–685.
- [45] Z. Li, L. Schulz, C. Ackley, N. Fenske, Adsorption of tetracycline on kaolinite with pH-dependent surface charges, *J. Colloid. Interf. Sci.*, 351(1) (2010) 254–260.

### Supporting file

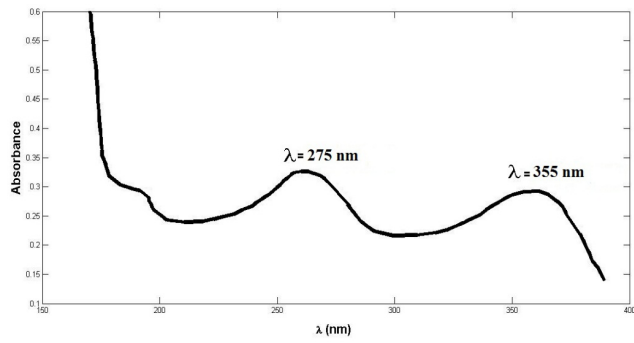


Fig S1. Uv-visible curve of tetracycline at the concentration of 20 ppm.

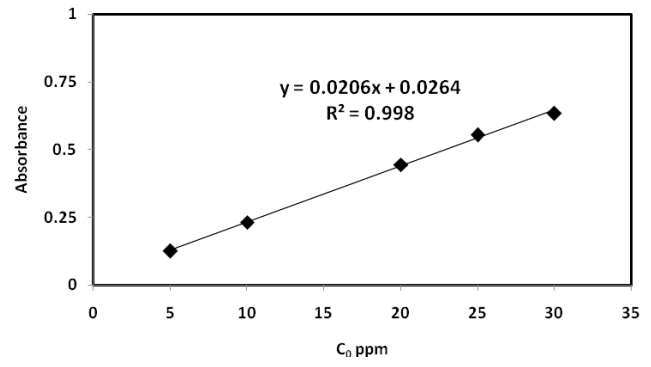


Fig S2. Calibration curve of tetracycline for UV visible analysis.